Physics of Plasmas ARTICLE pubs.aip.org/aip/pop

Ion-wake-mediated dust interactions under PK-4 conditions: A generalized and compact potential formulation

Cite as: Phys. Plasmas **33**, 093701 (2026); doi: 10.1063/5.0339932
Submitted: 21 April 2026 · Accepted: 27 August 2026 ·
Published Online: 16 September 2026

View Online Export Citation CrossMark

Diana Jimenez Marti,[1] Benny Rodriguez Saenz,[1] Peter Hartmann,[1,2] Evdokiya Kostadinova,[3] Truell Hyde,[1] and Lorin Swint Matthews[1,a)]

AFFILIATIONS

[1]Center for Astrophysics, Space Physics and Engineering Research (CASPER), Baylor University, Waco, Texas 76798-7310, USA
[2]Institute for Solid State Physics and Optics, Wigner Research Centre for Physics, 49, Budapest H-1525, Hungary
[3]Physics Department, Auburn University, Auburn, Alabama 36849, USA

[a)]**Author to whom correspondence should be addressed:** lorin_matthews@baylor.edu

ABSTRACT

Under microgravity conditions, dust particles in a plasma have been observed to self-organize into string-like structures. The mechanisms that lead to the formation of these structures are not yet fully understood. Interactions between charged dust particles and ion wakes have been proposed as a possible mechanism driving this self-organization process. To examine how plasma conditions associated with ionization waves affect ion wake properties and the resulting dust structures, we develop a general effective potential model for dust and ion wake systems under PK-4-like conditions. The electric potential is represented as the sum of a negative screened Coulomb term and a positive Gaussian contribution. Using a fixed and reduced set of coefficients determined from molecular dynamics simulations, the model captures the main features of the wake-modified potential for multiple dust arrangements containing different numbers of dust particles. Its implementation in a small-scale dust dynamics simulation further demonstrates its applicability to the study of ion-wake-mediated dust dynamics. The characteristics of the ionization waves in the DC discharge are shown to play an important role in determining the properties of the ion wakes and the resulting dust structure.

Published under an exclusive license by AIP Publishing. https://doi.org/10.1063/5.0339932

16 September 2026 10:23:49

I. INTRODUCTION

Dusty plasmas provide a platform to explore new physical phenomena connecting different areas of physics. Dusty (complex) plasmas consist of a three-component plasma—electrons, ions, and neutral particles—with suspended dust particles, typically ranging in size from nanometers to micrometers. When immersed in a plasma, these particles acquire electric charge, primarily through the collection of ions and electrons.[1] Since electrons have higher mobility, the net charge of the dust is predominantly negative. Charged dust grains in a plasma environment behave as an additional plasma constituent. Because of the very low charge-to-mass ratio of dust grains, their dynamic timescales are much slower compared to other plasma species. In addition, their macroscopic dimensions allow these particles to easily be observed and imaged, turning them into a powerful tool to investigate the dynamics of each particle and the system at the kinetic level.

One interesting feature is the formation of ordered dust structures, which has been widely reported in experiments.[2–6] The PlasmaKristall-4 (PK-4) system onboard the International Space Station (ISS) has been employed to carry out dusty plasma experiments under microgravity conditions since 2014.[7] Experiments performed in this facility have shown the formation of dust string-like structures parallel to the direction of the axial electric field.[2,3] This electrorheological (ER) behavior of dusty plasmas enhances their relevance as a system for theoretical and experimental research.[8,9] ER fluids consist of microparticles suspended in a nonconducting fluid which has a different dielectric constant from that of the particles. In such systems, an external electric field polarizes the particles, leading to a dipole–dipole coupling between them. Because of the dipole-dipole interaction, particles organize into strongly coupled structures such as crystals, sheets, and chains. In ER dusty plasmas, the polarization arises from the distortion of the Debye shielding cloud surrounding the negatively charged dust particles. However, the specific processes responsible for the formation of these structures are still not fully known and constitute an active field of research.

Published under an exclusive license by AIP Publishing

Under the action of an external electric field, positive ions acquire a net drift velocity in the direction of the electric field. The attractive electric force of a negatively charged dust grain acting on the streaming ions leads to the formation of an ion wake, a region of enhanced ion density downstream of the grain, along the ion streaming direction. The attractive electric interaction between dust and ion wakes has been proposed as one of the mechanisms leading to the formation of dust filaments.[10]

The location of the ion wake depends on the type of experiment. In ground-based experiments conducted in a Gaseous Electronic Conference radio frequency (GEC rf) cell, an external electric field frequency of 13.56 MHz is usually used.[11,12] Dust is levitated against gravity by the electric field in the plasma sheath above the lower electrode. Ions are accelerated from the bulk and flow toward the lower electrode. Hence, the ion wake is formed below the dust grain [see Figs. 1(a) and 1(c)]. In contrast, in experiments under microgravity conditions such as the PK-4 DC plasma, an alternating electric field is used to confine the dust grains in the field of view with a typical frequency of 500 Hz.[2,8] In this case, the ions can respond to the changing direction of the electric field, leading to ion density enhancements on both sides of the dust grain [Figs. 1(b) and 1(d)].

The local plasma parameters in the PK-4 discharge, computed using a two-dimensional particle-in-cell with Monte Carlo Collisions (PIC/MCC) simulation, exhibit quasiperiodic moving inhomogeneities, known as ionization waves.[13] The fluctuations of the electric field intensity and the electron and ion number densities in these waves can reach amplitudes up to ten times their time-averaged value. Simulations presented in Ref. 14, in which dust charging and the coupled dynamics of ions and dust grains were modeled, showed that the high electric field intensity associated with the ionization waves are an important factor behind the formation of the string-like dust structures observed in the PK-4 experiment.

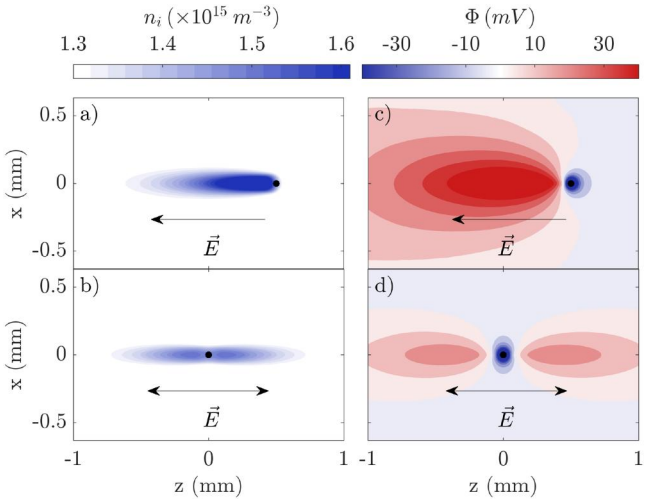


FIG. 1. Illustrative representation of the ion density [(a) and (b)] and electric potential of a dust grain plus ion wake [(c) and (d)] for: [(a) and (c)] a unidirectional electric field and [(b) and (d)] a polarity-switching electric field. The positions of the dust grains are indicated by black dots. The quantities shown were obtained from a numerical simulation of ion dynamics around a fixed dust grain with representative plasma parameters and are included only to illustrate the relative ion wake location.

Several models have been developed to describe the electric potential of the ion wake, replacing explicit ion dynamics in large-scale simulations to reduce computational cost while preserving the key physics of dust-wake interactions. One of the simplest models is the so-called point charge model, in which the ion cloud is replaced by a positive point charge with a symmetric Yukawa potential. This approach has been widely used to investigate ground-based phenomena like the non-reciprocal interaction in vertically aligned grains,[15] charging of interacting dust grains,[16] dynamics of 2D and 3D normal modes,[17,18] among others. Other studies have been performed using a modified point charge model by also including the dipole moment term in the potential.[19,20] In Ref. 21, a kinetic approach is used to develop an interaction potential model for dust particles in plasmas, describing the potential of a point dust particle in a weakly ionized plasma with an ion drift driven by an external electric field. A Gaussian representation of the ion wake has also been used in several studies, which avoids the singularity that arises near the ion wake region in the point charge model.[22,23] In Ref. 22, this approach was used to identify minimum energy configurations for two and three dust grains under ground-based conditions. The wake-mediated potential for each dust particle is described by three adjustable coefficients, which are specific to the particle arrangement. Consequently, a different set of coefficients is required for each configuration, making the application of this model to dust dynamics simulations complex and time-consuming. In Ref. 23, a Gaussian-based model was employed to describe the differences in ion wakes formed under constant and time-evolving plasma conditions due to ionization waves under PK-4-like conditions. In this formulation, the number of coefficients also scales linearly with the number of dust grains (in this case determined for a chain of four dust grains separated at 250 μm) and is not transferable to other dust configurations.

In this work, we present a more robust and general potential model formulation for the electric potential distribution of the dust and ion wake system in the vicinity of dust chains in representative PK-4 environments. It uses a fixed, reduced set of coefficients that is independent of the number of dust particles. The coefficients are shown to be extendable to a wide variety of dust configurations, making it a versatile tool for complex plasma studies. We use a molecular dynamics code to simulate the motion of ions to determine the charging of dust and electric potential distribution near chains of dust grains under time-evolving plasma conditions to account for the influence of ionization waves. Four different interparticle distances are used to determine the fitting coefficients as dust grains approach each other, with the aim of making the model generalizable to dust arrangements beyond string-like configurations. The model was implemented in a small-scale dust dynamics simulation to demonstrate its practical applicability.

II. BACKGROUND

A. PK-4 experiment

The Plasmakristall-4 (PK-4) is a complex plasma experiment installed on the International Space Station (ISS). A detailed description of this experiment can be found in Refs. 7 and 24. This microgravity experiment (see Fig. 2) consists of a 30-mm diameter and

16 September 2026 10:23:49

Published under an exclusive license by AIP Publishing

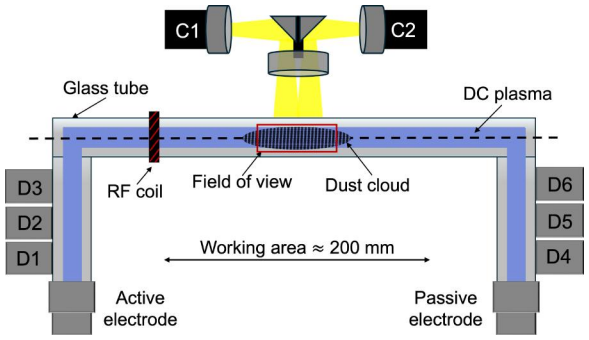


FIG. 2. Scheme of the PK-4 experimental setup.

400-mm length π-shaped glass tube. Two particle observation cameras (C1 and C2) are used to visualize the dust. Three dust shakers on each side of the tube (D1–D6) are used for dispensing the dust grains into the tube. The active and passive electrodes are located at the two ends of the tube. The experiment setup allows for the generation of a direct current (dc) or radio frequency (rf) plasma discharge with argon or neon gas and includes the option of polarity switching of the axial DC electric field to trap the charged dust grains in the working area (central region of the glass tube, 200-mm long). The polarity of the electrodes is alternated at a high enough frequency ($f = 500$ Hz) that the grains cannot respond to the change in the field direction (characteristic frequencies of the dust dynamics are in the range 10–100 Hz[25]).

B. Formation of dust filaments

It has been observed that dust grains under DC switching conditions can form long and stable filaments along the direction of the axial alternating electric field (see Fig. 3).[3] The average interparticle distance within a filament is typically around $200 - 350\ \mu$m.[3,14,26,27] The ions are light enough that they can respond to the change in polarity of the electric field and flow according to its direction. The ion trajectories are deflected by the negatively charged dust grains and form a region of enhanced ion density known as an ion wake (see Fig. 1). In the case of a unidirectional electric field, the ion density enhancement occurs behind the dust grain [Figs. 1(a) and 1(c)]. For a polarity-switching electric field, ion focusing alternates its direction, leading to an effective ion density enhancement on both sides of the grain [Figs. 1(b) and 1(d)]. The interaction between ion wakes and dust grains is the probable mechanism responsible for the formation of dust structures.[10,28]



FIG. 3. Dust filaments in the PK-4 experiment at 70.5 Pa neon gas pressure and 1 mA DC current. Reprinted with permission from Kostadinova *et al.*, AIAA Paper No. 2023-2615, 2023. Copyright 2023 American Institute of Aeronautics and Astronautics, Inc.[34]

C. Time-evolving plasma conditions

The local parameters in the PK-4 system are modeled with the axisymmetric 2D particle-in-cell with Monte Carlo Collisions (2D3V PIC/MCC) simulation presented in Ref. 13. The simulation domain consists of a 400 mm-long dielectric tube with a 30 mm inner diameter, resolved on a grid with 64 radial grid points and 2048 axial grid points. Approximately 10^7 macroparticles were used for each charged species. The gas temperature (T_g), discharge current (I) and DC voltage (V) used for simulations at 40 and 60 Pa neon gas pressures (p) are shown in Table I.[13,14] This model revealed the existence of quasiperiodic inhomogeneities moving along the axial direction within the positive column of the PK-4 discharge, known as ionization waves, which were confirmed by the ground-based experiments in PK4-BU.[13] Spatial profiles of the ion density and axial electric field for 40 and 60 Pa neutral gas pressures are shown in Fig. 4. The corresponding results for the rest of plasma parameters can be found in Refs. 13 and 14. Plasma parameters such as electron temperature (T_e), ion temperature (T_i), electron density (n_e) and ion density (n_i) were shown to vary by up to one order of magnitude as an ionization wave passes a given position within the discharge tube (Fig. 5). The ratio between the ion and electron density (n_i/n_e) obtained from the PIC/MCC simulation is shown in Fig. 6. These waves have a frequency of the order of 10 kHz. Although these timescales are much faster than the dust response time, these temporal variations in the plasma parameters have been shown to influence the dust ordering and ion wake features.[14,23]

III. METHODS

A. Dynamic response of ions and dust (DRIAD)

To simulate the ion dynamics and dust charging, we use the N-body molecular dynamics code DRIAD,[16] which resolves the equations of motion of these species according to their own timescales. The simulation does not directly model the electrons, which are instead treated as a fluid governed by a Boltzmann distribution that shields an ion's electric potential and determines the electron current to dust grains.[16] This assumption corresponds to electrons reaching

TABLE I. Parameters used in the PIC/MCC simulations of the PK-4 experiment (Input parameters) and time-averaged plasma parameters over the selected portion (Time-average output parameters) for 40 and 60 Pa gas pressures.

Pressure (Pa)	40	60
Input parameters		
T_g (meV)	25.9	25.9
I (mA)	0.8	2.0
V (V)	1000	770
Time-averaged output parameters		
$n_i(\times 10^{15}\mathrm{m}^{-3})$	0.219	1.26
$n_e(\times 10^{15}\mathrm{m}^{-3})$	0.197	1.25
T_i (meV)	39.3	43.1
T_e (meV)	6350	4300
$\lambda_{Di}(\mu\mathrm{m})$	99.7	43.4
$\lambda_{De}(\mu\mathrm{m})$	1336	435
$E_z(\mathrm{V/m})$	289	198
M	0.04	0.03

16 September 2026 10:23:49

Published under an exclusive license by AIP Publishing

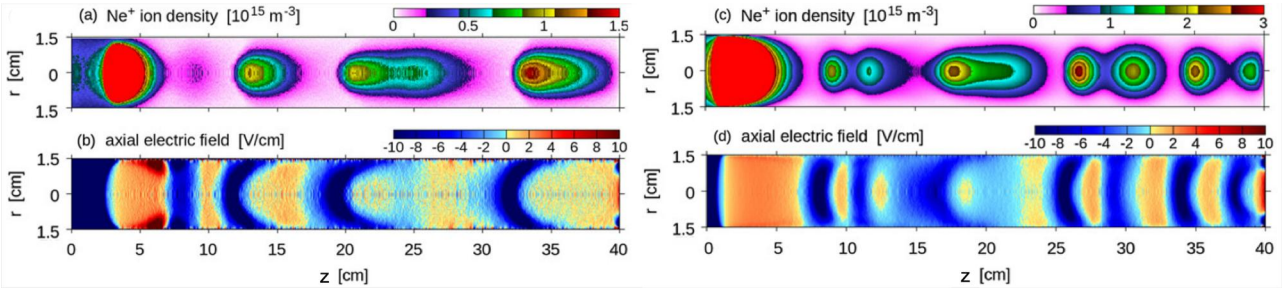


FIG. 4. Spatial profiles of the ion density [(a) and (c)] and axial electric field [(b) and (d)] across the simulation region from the PIC/MCC simulation for: [(a) and (b)] 40 and [(c) and (d)] 60 Pa.

equilibrium with the electrostatic potential on time scales much shorter than those of the ion and dust dynamics resolved in the simulation. Since dust grains are negatively charged, the Boltzmann relation predicts the electron depletion in the vicinity of the grain. We use the simulation to self-consistently obtain the charge on a fixed arrangement of dust grains and the distribution of ions in the vicinity of the dust. To enhance computational efficiency, we model the dynamics of superions, which are clusters of ions with the same charge-to-mass ratio as a single ion. The number of ions per superion is calculated as $n_i V_{sim}/N_{si}$, where n_i is the ion number density, V_{sim} is the simulation volume and N_{si} is the number of superions used in the simulation. The superions that leave the simulation region or are collected by a dust grain are re-injected with random positions and velocities on the boundary consistent with the ion drift speed, following the method presented in Ref. 29.

The equation of motion for the ions (with mass m_i) is

$$m_i \ddot{\vec{r}}_i = \vec{F}_{iD} + \vec{F}_{ii} + \vec{F}_{bound} + \vec{F}_z + \vec{F}_{in}. \tag{1}$$

The first term on the right-hand side represents the force on an ion i with charge q_i due to dust grains with charge Q_d located at a distance $|\vec{r}_{id}|$ from the ion, which is described by a Coulomb interaction [Eq. (2)], as electrons are depleted in the vicinity of the negatively charged dust grain and the ions modeled in the simulation provide the Debye shielding

$$\vec{F}_{iD} = \sum_{d=1}^{N_D} \frac{q_i Q_d}{4\pi\epsilon_0} \frac{\vec{r}_{id}}{|\vec{r}_{id}|^3}. \tag{2}$$

The force from other ions inside the simulation $\vec{F}_{ii}$ is given by a screened Coulomb interaction to account for the screening provided by the electrons

$$\vec{F}_{ii} = \sum_{j\neq i}^{N_i} \frac{q_i q_j}{4\pi\epsilon_0} \left(1 + \frac{|\vec{r}_{ij}|}{\lambda_{De}}\right) \exp\left[-\frac{|\vec{r}_{ij}|}{\lambda_{De}}\right] \frac{\vec{r}_{ij}}{|\vec{r}_{ij}|^3}, \tag{3}$$

where $q_{i,j}$ is the charge of the ions i, j, separated by the distance $|\vec{r}_{ij}|$ and $\lambda_{De} = \sqrt{\epsilon_0 k_B T_e/(n_e e^2)}$ is the electron Debye length.

The confining electric force $\vec{F}_{bound} = q_i \vec{E}_{bound}$ arises from the electric field $\vec{E}_{bound}$ due the ions outside the simulation region. This field is derived from the gradient of the potential distribution within an empty cylindrical cavity that matches the dimensions of the simulation region immersed in a uniform plasma with density n_o,

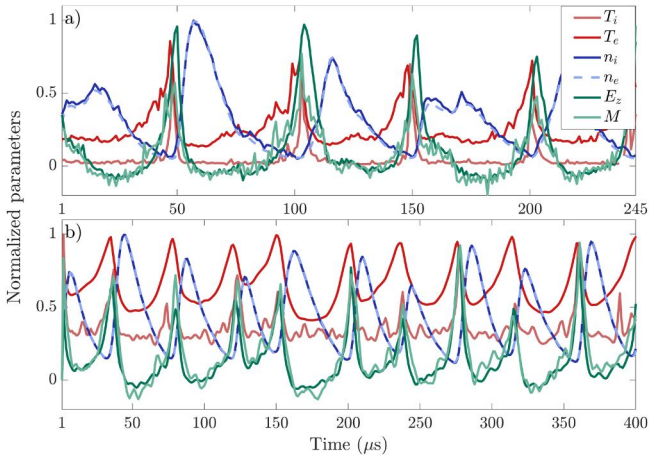


FIG. 5. Representative segment of the time-evolving plasma parameters obtained from the PIC/MCC simulation at the center of the simulation domain ($r = 0$ cm, $z = 20$ cm), at (a) 40 and (b) 60 Pa. All magnitudes are normalized by their corresponding maxima.

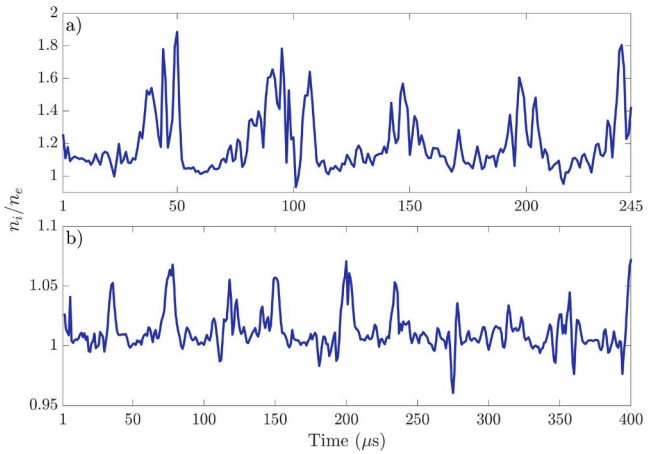


FIG. 6. Ratio of ion to electron number density (n_i/n_e) obtained from the PIC/MCC simulation at the center of the simulation domain ($r = 0$ cm, $z = 20$ cm), at (a) 40 and (b) 60 Pa.

16 September 2026 10:23:49

Published under an exclusive license by AIP Publishing

representing the density far from the simulated region. The force $\vec{F}_z = q_i \vec{E}_z$ originates from the interaction of the ions with the axial electric field $E_z\hat{z}$. $\vec{F}_{in}$ is the force due to the ion-neutral collisions, which is calculated using the null-collision method. Ion-neutral collisions affect the ion wake formation by modifying the downstream ion focusing behind the dust grains. In collisionless flows, ions can follow more coherent trajectories along the flow direction, producing more elongated wakes. In contrast, ion-neutral collisions interrupt the directed ion motion, leading to more compact wakes, as shown in Couëdel *et al.*[30]

In order to account for the effects of the time-evolving plasma conditions due to the ionization waves, plasma conditions from a point at the center of the PIC/MCC simulation are modeled, which includes data of the ion temperature (T_i), ion number density (n_i), electron temperature (T_e), electron number density (n_e), axial electric field (E_z) and Mach number (M), defined as $M = v_{i,z}/v_B$, where $v_{i,z}$ is the drift velocity of the ions in the z-direction and $v_B = \sqrt{k_B T_e/m_i}$ is the Bohm velocity. A portion of these evolving conditions (covering two ionization waves, blue-shaded areas in Fig. 7) is used to provide repeated boundary conditions. The segment has a duration of 106 μs in the 40 Pa case and 86 μs for 60 Pa. Figure 8 shows a 600 μs representative segment of the axial electric field in its original units (non-normalized) for both the 40 and 60 Pa conditions. The direction of the electric field is reversed every half-cycle ($1/2f = 1$ ms). The rest of the plasma parameters are repeated cyclically through the simulation. The time-average of each plasma parameter over the selected portion of the PIC/MCC simulation are detailed in Table I. The average electron and ion Debye lengths (λ_{De}, λ_{Di}) are calculated using the corresponding average number density and temperature.

B. Ion wake and dust potential model

The spatial distribution of the electric potential can be used to propose a model for the potential of dust mediated by the ion wake in filamentary structures. Because the ion wakes are aligned in the axial direction, the electric potential distribution around the dust chains exhibits approximate axial symmetry. Under these circumstances, the

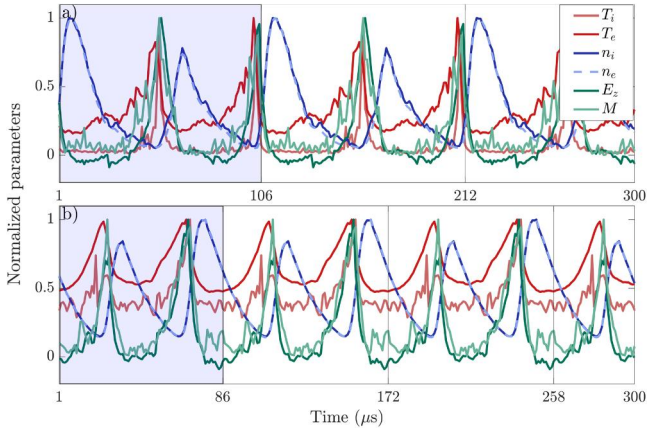


FIG. 7. Representative segment of the time-evolving plasma parameters used in the simulation at (a) 40 and (b) 60 Pa, covering a 300 μs time interval. The selected portion from the PIC/MCC simulation (blue-shaded area) is repeated cyclically. All magnitudes are normalized by their corresponding maxima.

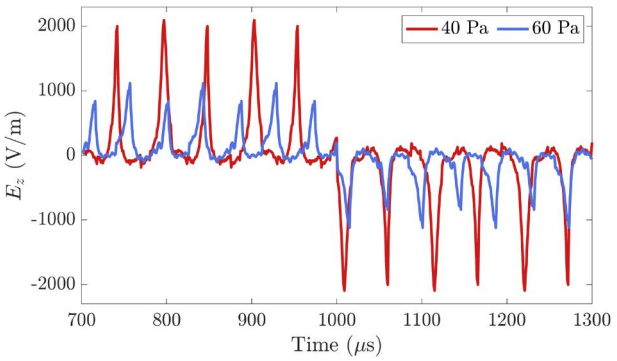


FIG. 8. Representative segment of the time-evolving axial electric field (E_z) used in the simulation, covering a 600 μs time interval. The polarity of the electric field switches at $t = 1000$ μs.

variations in the azimuthal direction are negligible compared with the radial and axial variations, making any slice that contains a chain of dust grains representative of the full three-dimensional structure. For this reason, the analysis focuses on data on the xz plane, where the most relevant features of the potential are fully captured. Consequently, the model will be formulated directly in two dimensions, which preserves all physically significant information while increasing the stability of the fitting procedure.

Figure 9 shows a representative electric potential along the z axis for a chain of four dust grains located along the cylinder axis, under 60 Pa gas pressure, a discharge current of 2.0 mA and a DC voltage of 770 V.[23] As expected for negatively charged dust particles, the potential exhibits highly negative values near the dust grain and increases rapidly toward zero as the distance from the dust grains increases, interpreted as the presence of a term in the potential model that is negative and inversely proportional to the distance from each grain. Between the grains, one sees the presence of elevated electric potential (local maxima), suggesting the presence of a positive contribution to the electric potential from the ion wake. As the electric potential approaches zero at long distances, both contributions should be decaying functions. Considering these aspects, we propose a potential

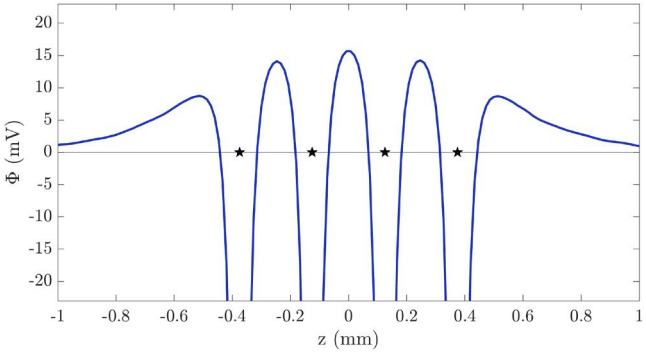


FIG. 9. Electric potential at ($x = 0$, z) for a chain of four dust grains located along the cylinder axis, separated by a distance $\Delta = 250$ μm ($p = 60$ Pa, $T_g = 25.9$ meV, $V = 770$ V). Positions of the dust grains are indicated by black stars.

16 September 2026 10:23:49

Published under an exclusive license by AIP Publishing

model consisting of a screened Coulomb potential from each grain and an anisotropic Gaussian function centered at each dust grain,

$$\Phi(x,z)=\sum_{d=1}^{N_D}\left[\frac{Q_d}{4\pi\epsilon_0}\frac{e^{-|\vec{r}-\vec{r}_d|/\lambda_d}}{|\vec{r}-\vec{r}_d|}+\alpha_d\frac{|Q_d|}{4\pi\epsilon_0}e^{-\left[\frac{x-x_d}{\sigma_{x,d}}\right]^2}e^{-\left[\frac{z-z_d}{\sigma_{z,d}}\right]^2}\right], \quad (4)$$

where Q_d and $\vec{r}_d=(x_d,z_d)$ are the charge and position vector of the d-th dust grain and N_D is the number of dust grains. The coefficients λ_d, α_d, $\sigma_{x,d}$, and $\sigma_{z,d}$ are all positive. The coefficient λ_d represents the isotropic shielding of the negative dust grain by the ions. A small value of this coefficient represents a greater isotropic shielding. The coefficient α_d represents the scaling factor for the positive contribution to the wake potential. A greater value of this coefficient indicates a stronger ion wake. The coefficients $\sigma_{x,d}$ and $\sigma_{z,d}$ control the decay of this positive contribution in the x and z directions, respectively. A smaller value for these parameters represents a shorter decay length. This potential model is a modified and more general version of the model presented in Ref. 23. In the present case, we include the absolute value of the charge as a multiplicative factor that controls the maximum of the Gaussian term along with the coefficient α_d. This takes into account that a higher dust charge implies that more ions will be focused on the ion wake for a given external electric field, density, and pressure, resulting in a more prominent ion wake. The present formulation of the model improves its generalizability, which will be addressed in Secs. V A and V B.

This model for the potential can be naturally extended to three dimensions [Eq. (5)] by including a y-dependent term and an extra coefficient $\sigma_{y,d}$ in the asymmetric Gaussian in Eq. (4). Coefficients $\sigma_{x,d}$ and $\sigma_{y,d}$ are expected to be equal due to the symmetry of the system around the z-axis. The two-dimensional case [Eq. (4)] is recovered when Eq. (5) is evaluated at $y=0$, $y_d=0$ (xz plane).

$$\Phi(x,y,z)=\sum_{d=1}^{N_D}\left[\frac{Q_d}{4\pi\epsilon_0}\frac{e^{-|\vec{r}-\vec{r}_d|/\lambda_d}}{|\vec{r}-\vec{r}_d|}+\alpha_d\frac{|Q_d|}{4\pi\epsilon_0}e^{-\left[\frac{x-x_d}{\sigma_{x,d}}\right]^2}e^{-\left[\frac{y-y_d}{\sigma_{y,d}}\right]^2}e^{-\left[\frac{z-z_d}{\sigma_{z,d}}\right]^2}\right]. \quad (5)$$

IV. RESULTS

A. Numerical modeling

To examine the electric potential distribution near a dust chain and determine how the model coefficients evolve as dust grains approach each other, we conducted simulations with DRIAD using chains of four melamine formaldehyde (MF) spherical dust grains with radius $R_D=1.69\,\mu$m under 40 and 60 Pa neon gas pressures. The neutral gas temperature is 25.9 meV. The dust mass is 3.05×10^{-14} kg according to its radius and density (1510 kg/m^3). Four different cases were examined, corresponding to the interparticle distances $\Delta=250$, 350, 450, and 550 μm. The number of superions considered in the simulations is 150 000 and 100 000, respectively. The simulation geometry for both pressures is a cylinder of radius $2.0\lambda_{De}$, while the length was set to $6.0\lambda_{De}$ (8.02 mm) at 40 Pa and $12\lambda_{De}$ (5.22 mm) at 60 Pa. These cylinder sizes and number of superions were chosen to ensure that dust particles remain at least $2.0\lambda_{De}$ away from the simulation boundaries and that each superion has about 200 ions in both cases. From the spatial profiles of the ionization waves (Fig. 4), the distance between consecutive peaks is estimated to be in the range of 5–10 cm. Therefore, the simulation domain is much smaller than the wavelength of the ionization waves. The ion time step is $\Delta t_i=0.01\mu$s. For reference, the ion plasma frequency ω_i under these conditions is of order 10^6 rad/s, with estimated values of $\omega_i\approx4.35\times10^6$ rad/s for the 40 Pa case and $\omega_i\approx10.4\times10^6$ rad/s for 60 Pa. The representative segments in the shaded areas shown in Fig. 7 from the PIC/MCC simulation are used to account for the time-evolving boundary conditions in the simulation for the two pressures. The evolving plasma parameters are updated every 1 μs (100 ion time steps). The external electric field $\vec{E}_z$, in the axial direction, switches direction every 1 ms given $f=500$ Hz with a 50% duty cycle. The total time simulated is 600 ms. The resulting ion electric potential and dust charge are averaged over the last 580 ms after the system is in equilibrium, covering 290 complete cycles of the switching electric field.

Figure 10 shows the ion density distributions of the ion wake (n_w) from the simulations at each interparticle distance (Δ) under both pressures. These distributions were calculated by subtracting the ion density of the simulation without dust particles from that of each case, in order to isolate the ion distribution caused by the presence of the dust. The average charge of the dust grains at equilibrium is shown in Fig. 11 for both pressures as a function of the dust position. The charge fluctuations, quantified as the relative standard deviation $\sigma_Q/\langle Q_d\rangle$ for each dust particle, remained within 5.0%–12% across all cases. The dust charge at 40 Pa is about 15% lower than at 60 Pa. In the 40 Pa case, ions have a slightly lower temperature, making it easier to capture them. In addition, there is a greater difference between the average electron and ion number densities n_e and n_i (see Fig. 6 and Table I), implying an enhanced ion current for this pressure. Together, these effects increase the probability of capturing ions. In a given chain, the two inner dust grains tend to collect less negative charge than the two outer dust grains, with a more marked difference in the 40 Pa cases, since the ion current is enhanced in this region. This difference increases as Δ decreases since the ion density is enhanced as dust grains move closer (see Fig. 10). The dust charge tends toward that for an isolated grain as Δ increases. This is an expected result since ions approaching a given grain experience a reduced influence from neighboring grains. As a result, each grain charges under conditions that are increasingly independent and are closer to the single dust case.

The electric potential maps are shown in Fig. 12. The potential distributions show a highly negative potential in the region close to the dust grains. In the 40 Pa cases [Figs. 12(a)–12(d)] the potential takes small positive values between the farthest spaced grains [Fig. 12(a)] and becomes more negative as grains approach each other [Fig. 12(d)]. On the other hand, the potential in the 60 Pa cases [Figs. 12(e)–12(h)] reaches positive values between dust grains and becomes more positive as Δ decreases. This is consistent with a higher ion density in the 60 Pa case compared to the 40 Pa case (see Table I).

V. ANALYSIS AND DISCUSSION

A. Data-driven model simplifications

The potential model Eq. (4) is formulated with independent coefficients for each dust grain and for each interparticle distance, yielding a total of 64 free coefficients (4 parameters per dust grain $\times$ 4 dust grains $\times$ 4 configurations) for each pressure. The resulting

16 September 2026 10:23:49

Published under an exclusive license by AIP Publishing

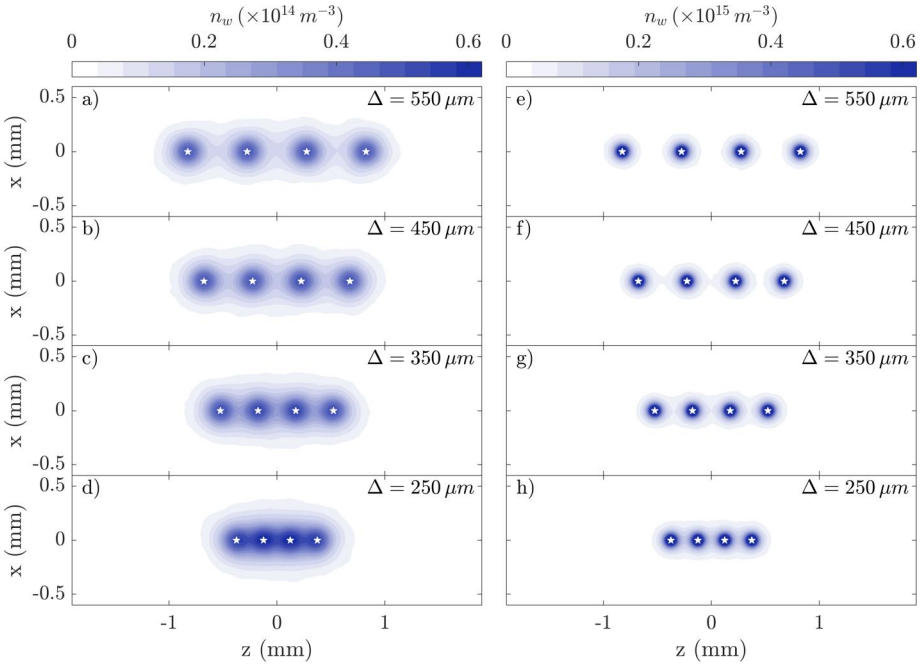


FIG. 10. Ion density distribution of the ion wake obtained from DRIAD for: (a)–(d) 40 and (e)–(h) 60 Pa gas pressure. The positions of the dust grains are represented by white stars.

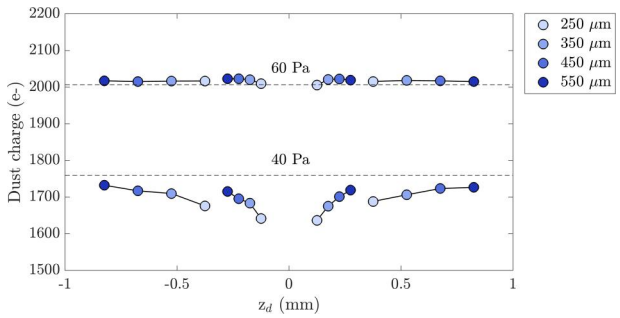


FIG. 11. Charges of the four dust grains for 40 and 60 Pa pressures as a function of the dust position. Marker colors indicate the different cases considered, corresponding to a specific interparticle distance. The horizontal dashed lines represent the charge obtained from simulations for a single dust grain at each pressure.

coefficients from preliminary fittings of this fully independent formulation to the data showed no significant variation in the coefficients for grains within the same chain and only minor differences between configurations. Moreover, no trend was observed with the interparticle distance, i.e., the coefficients did not exhibit a consistent increase or decrease as Δ changed. As shown in Fig. 12, the functional shape of the potential is essentially the same in all cases for a given pressure. The only noticeable difference is a gradual change in the ion wake intensity as the interparticle distance decreases. The ion wake intensity is regulated by the dust charge (the higher the absolute value of the charge, the more ions are attracted by the dust grain) and by the distance between the grains, since wakes tend to overlap more strongly as the particles move closer together. This dependence is already built into the potential model, where the wake intensity scales proportionally with charge and depends explicitly on the particle positions. The Mach number of the ion flow also influences the wake intensity by controlling the degree of ion focusing behind the grain. Since all four simulations considered for each pressure were performed using the same plasma conditions, the flow regime remains the same across cases for a given pressure. Such numerical behavior suggests that the additional degrees of freedom might not correspond to real physical differences, but rather to redundant parameters within the model.

Guided by these results, the model was progressively simplified in two steps. First, the coefficients were assumed to be identical for all grains within a chain ($\alpha_d = \alpha$, $\sigma_{x,d} = \sigma_x$, $\sigma_{z,d} = \sigma_z$, $\lambda_d = \lambda$). Second, the same set of coefficients was extended to all cases for a given pressure. This two-step simplification reduced the number of free parameters from 64 to only 4 for each pressure, resulting in a more compact formulation. This reduction greatly improves the numerical stability of the fitting process while preserving the model's ability to capture the essential features of the data. The resulting analytical form of the potential model after these simplifications is

$$\Phi(x,z) = \sum_{d=1}^{N_D}\left[\frac{Q_d}{4\pi\epsilon_0}\frac{e^{-|\vec{r}-\vec{r}_d|/\lambda}}{|\vec{r}-\vec{r}_d|} + \alpha\frac{|Q_d|}{4\pi\epsilon_0}e^{-\left[\frac{x-x_d}{\sigma_x}\right]^2}e^{-\left[\frac{z-z_d}{\sigma_z}\right]^2}\right]. \quad (6)$$

B. Potential model fitting

The positions of N_D equally spaced dust grains in a chain arranged symmetrically about the origin along the z-axis ($x_d = 0$, $y_d = 0$) can be fully described by the interparticle distance instead of their four individual positions. For practical implementation, the simplified expression of the potential model Eq. (6) was written in terms of the interparticle distance Δ rather than the positions of the dust grains as

16 September 2026 10:23:49

Published under an exclusive license by AIP Publishing

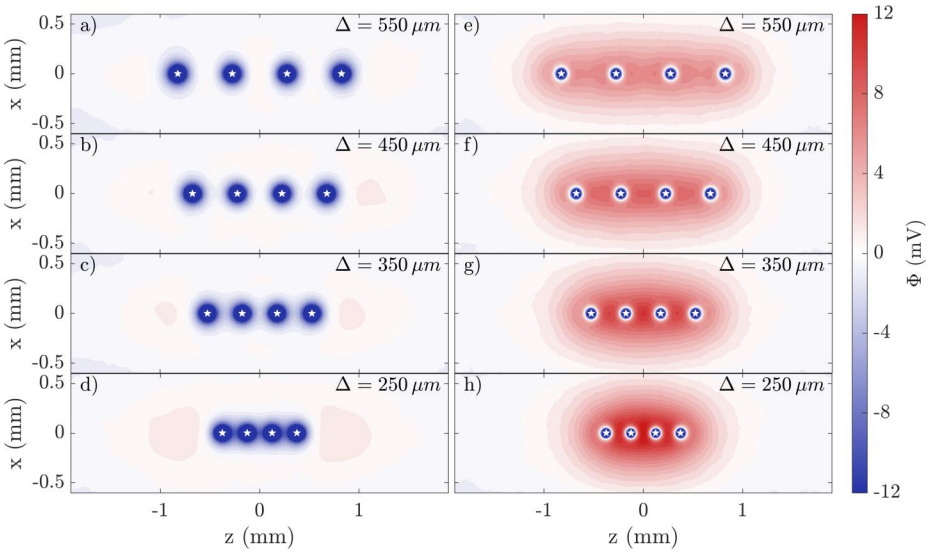


FIG. 12. Potential distribution for the dust and ion wake system obtained from DRIAD for: (a)–(d) 40 and (e)–(h) 60 Pa gas pressure. The positions of the dust grains are represented by white stars.

$$\Phi(x,z)=\sum_{d=1}^{N_D}\left[\frac{Q_d}{4\pi\epsilon_0}\frac{e^{\frac{-\sqrt{x^2+(z-k_d\Delta)^2}}{\lambda}}}{\sqrt{x^2+(z-k_d\Delta)^2}}+\alpha\frac{|Q_d|}{4\pi\epsilon_0}e^{-\left[\frac{x}{\sigma_x}\right]^2}e^{-\left[\frac{z-k_d\Delta}{\sigma_z}\right]^2}\right], \quad (7)$$

$$k_d=-\frac{2d-N_D-1}{2}.$$

This choice was made purely for computational simplicity, since expressing the potential model as a function of Δ reduces the number of input parameters required by the fitting routine. In order to determine the model coefficients, we fit the expression Eq. (7) to the data obtained from DRIAD (Fig. 12). In general, it is important to prevent the model from overfitting the data, as this compromises its generalizability and degrades its performance when applied to different conditions.[31] To prevent these limitations, we used the Leave-p-Out Cross-Validation (LpO CV) technique.[32] In this method, the data (which includes n samples) is split into a training set and a validation set (p samples). The training set ($n-p$ samples) is the data that is used in the model fitting to determine the coefficients. The validation set is not employed in obtaining the coefficients and is used just to evaluate the quality of the fit. This procedure is repeated until all possible subsets of size p have been used for validation. As a result, multiple sets of coefficients [specifically, $n!/(n-p)!p!$ sets] are obtained from the different fitting cases. Here we define the resulting model coefficients as the set for which the validation data are reproduced with the highest Coefficient of Determination (R^2), which was calculated according to Ref. 33. The implementation of the LpO CV method supports the model's generalizability to new dust configurations.

In this specific case, we used the $n=4$ data sets for each pressure to generate all possible combinations of $p=2$ validation sets. The remaining $n-p=2$ sets for a given combination were used as training sets. As a result, six sets of coefficients were obtained from the different fitting cases. Exploratory fittings were performed to identify the order of the coefficients. Based on this, normalizations were applied to the potential expression to bring all coefficients to the order of 1.0 and improve numerical stability during the fitting. The original coefficients were then recovered by reversing the normalizations.

The potential distributions obtained from the model Eq. (6) are shown in Fig. 13. The potential closely reproduces the simulation data in the entire simulation region. These results appear smoother and do not exhibit the variations caused by numerical noise observed in the simulated data.

The absolute value of the differences between the potential distribution predicted by the model Eq. (6) and the data obtained from the simulation (Fig. 12) is shown in Fig. 14 for the eight cases under consideration. Table II shows the values of R^2 and Root Mean Squared Error (RMSE). The difference plot indicates a good agreement between the data and the model, as the maximum absolute differences remain below 2 mV in all the cases. These differences are small when compared to the maximum absolute value of the potential in the vicinity of the dust grains (∼31 mV for 40 Pa and ∼12 mV for 60 Pa) and the dust surface potential (−1.4 V for 40 Pa and −1.7 V for 60 Pa). The values of R^2 remain above 99% and the RMSE is below 0.5 mV for all the cases. This suggests that the model accurately reproduces the fundamental features of the data. The potential in the vicinity of the dust grains is more accurately represented in the 40 Pa cases, as the difference is less in this region. For both pressures, the absolute deviation between the model and the simulation data increases as the interparticle distance decreases. When particles are separated at longer distances, local errors around each dust grain contribute independently to the absolute difference maps. As the interparticle distance decreases, these errors spatially overlap, leading to a higher discrepancy between the model and the data.

Table III presents the original coefficients obtained for both pressures and the ratio between them to compare the characteristics of the ion wakes and evaluate how their properties vary for the two pressures. The obtained coefficients are valid only for the set of plasma conditions considered in the simulations, including the pressure, ion density, electric field strength, particle size, and Mach number. For different plasma conditions, a new set of coefficients must be determined using simulations performed with the corresponding parameters. According to Table III, the coefficient λ is greater at 40 Pa than at 60 Pa, implying a stronger symmetric shielding of the dust at

16 September 2026 10:23:49

Published under an exclusive license by AIP Publishing

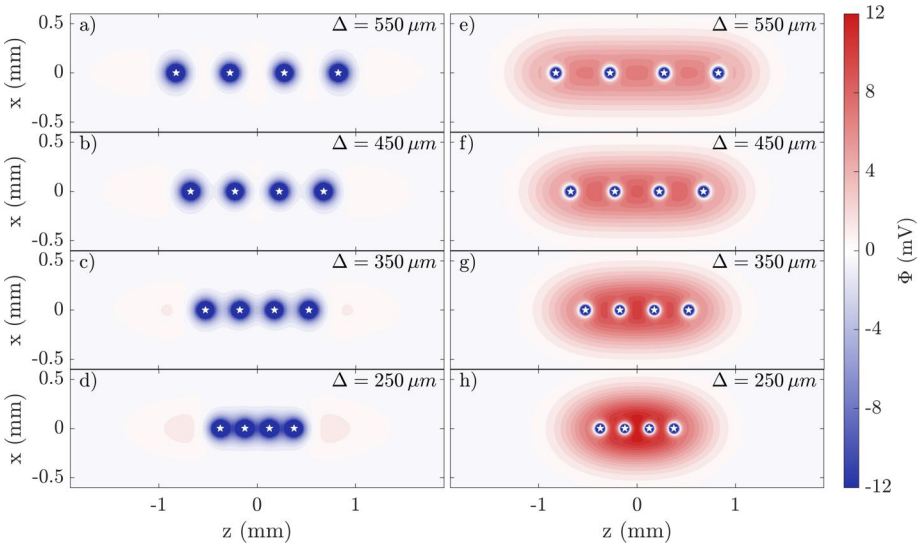


FIG. 13. Potential distribution obtained with the potential model in Eq. (6) for: (a)–(d) 40 and (e)–(h) 60 Pa gas pressure. The positions of the dust grains are represented by gray stars.

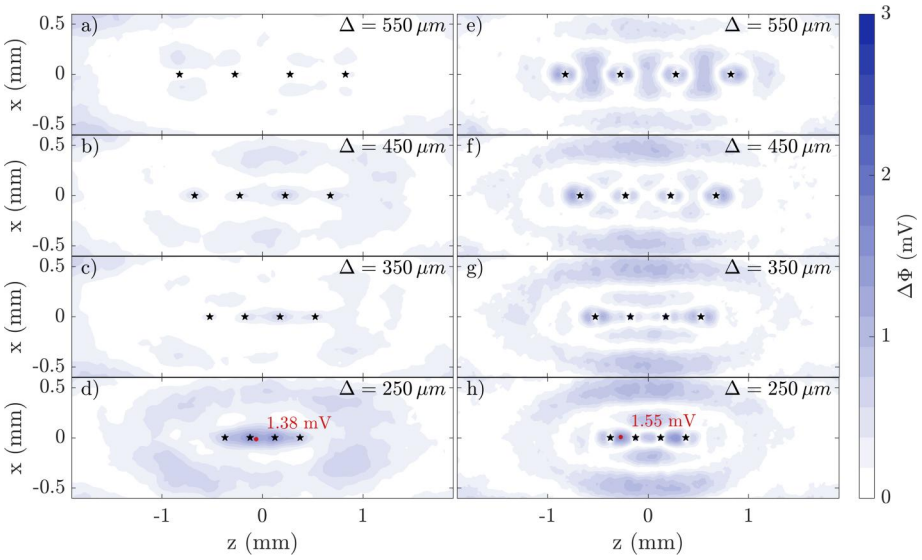


FIG. 14. Absolute difference between the potential distribution obtained with the potential model in Eq. (6) and the data obtained from DRIAD for: (a)–(d) 40 and (e)–(h) 60 Pa gas pressure. The positions of the dust grains are indicated by black stars. The red dot indicates the position where the maximum difference is reached, while the adjacent red label shows its value.

TABLE II. Coefficient of Determination (R^2) and Root Mean Squared Error (RMSE) for the training cases.

	40 Pa		60 Pa	
Δ (μm)	R^2 (%)	RMSE (mV)	R^2 (%)	RMSE (mV)
550	99.91	0.212	99.82	0.323
450	99.88	0.238	99.80	0.349
350	99.90	0.214	99.75	0.383
250	99.52	0.386	99.71	0.416

TABLE III. Coefficients obtained from data fitting for 40 and 60 Pa gas pressures, and the ratios of the values for the two cases (C_{40}/C_{60}).

	40 Pa	60 Pa.	C_{40}/C_{60}
α (m^{-1})	400	1760	0.227
σ_x (μm)	284	337	0.842
σ_z (μm)	840	436	1.93
λ (μm)	114	41.5	2.76
σ_z/σ_x	2.96	1.29	…

60 Pa pressure. The scaling factor for the positive contribution α is greater for the 60 Pa case than for the 40 Pa case, indicating a stronger ion wake at 60 Pa. This agrees with the higher ion density and lower Mach number obtained in the PIC/MCC simulation for the higher pressure (see Table I). The ratio between the coefficients σ_z and σ_x quantifies the degree of asymmetry of the ion wake and the direction of its elongation. For 60 Pa, the value of σ_z/σ_x is slightly greater than 1, suggesting an ion wake that is approximately circular but

16 September 2026 10:23:49

Published under an exclusive license by AIP Publishing

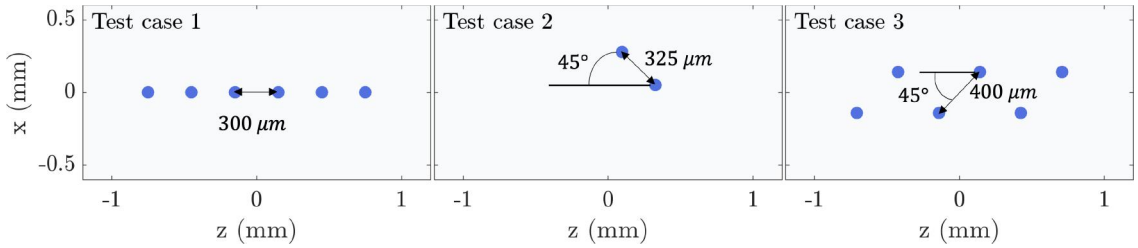


FIG. 15. Schematic representation of the dust configurations used as test cases.

moderately elongated along the axial direction. At 40 Pa, this ratio is significantly greater than 1, revealing a much more pronounced elongation. This behavior is consistent with the stronger axial electric field in this case compared to the 60 Pa case (see Fig. 8).

C. Potential model evaluation on independent test cases

We assess the generalizability of the potential model by applying it to test cases. We consider configurations that differ significantly from the ones used in determining the coefficients, with different particle numbers, interparticle spacing, and orientation relative to the direction of the ion flow. These structures also correspond to physically relevant dust arrangements observed in complex plasmas, such as interacting dust-grain pairs, filaments, and zigzag chains. These cases allow us to verify whether the model and the assumptions made remain valid for different scenarios and can accurately reproduce the electric potential distribution for a variety of relative dust positions. We used DRIAD to simulate the cases shown in Fig. 15: a chain of six dust grains with $\Delta = 300\,\mu$m (Test case 1), two dust grains separated by $\Delta = 325\,\mu$m but at an angle to the axial electric field direction (Test case 2), and a six-grain zigzag chain with $\Delta = 400\,\mu$m (Test case 3), with the same simulation parameters as the training cases.

The electric potential distributions obtained from DRIAD for the test cases are presented in Fig. 16 for both pressures. The potential maps generated by the model Eq. (6), using the coefficients from Table III and the dust charges predicted by DRIAD, are displayed in Fig. 17. The potential model reproduces the main features of the electric potential distribution with good accuracy for all the test cases, with differences below 2.0 mV (see Fig. 18), confirming that the simplified model closely matches the simulation data. Table IV presents the R^2 and RMSE values for all test cases. The R^2 values are above 99%, indicating that the model reproduces the test cases with high accuracy. The low RMSE values (mostly below 0.5 mV) also confirm the validity of the predictions, suggesting that the model effectively captures the trends in a variety of scenarios.

D. Implementation of the potential model in dust dynamics simulation

We test the utility of the potential model in a simple particle dynamics simulation. The simulation consists of eight dust grains with radius $R_D = 1.69\mu$m and mass $m_D = 3.05 \times 10^{-14}$ kg, matching those used in the DRIAD simulations presented in Secs. IV A and V C. Larger dust clouds will be investigated in future work using GPU-accelerated codes. For simplicity, we assume a uniform charge for all dust grains, corresponding to the charge obtained from the single-grain DRIAD simulation at each pressure ($Q_D = 1760e^-$ for 40 Pa and $Q_D = 2007e^-$ for 60 Pa). As shown in Fig. 11, dust charge depends on the interparticle distance, an effect that will be addressed in future work. The equation of motion of the dust grains is:

$$m_D\ddot{\vec{r}}_d = \vec{F}_{D,d} + \vec{F}_z + \vec{F}_n + \vec{F}_B. \tag{8}$$

The dust–dust interaction $\vec{F}_D$ is calculated using the three-dimensional form of the potential model given in Eq. (6), with the coefficients listed in Table III

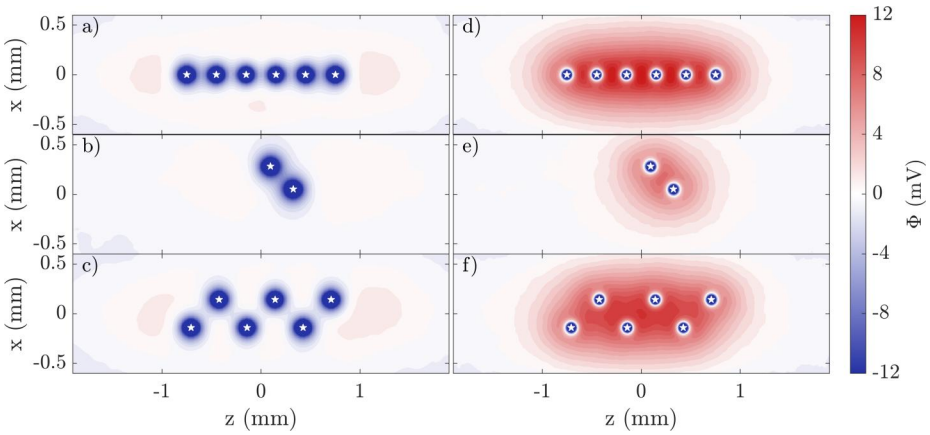


FIG. 16. Electric potential distribution obtained from DRIAD for the test cases under: (a)–(c) 40 and (d)–(f) 60 Pa gas pressures. The positions of the dust grains are indicated by white stars.

16 September 2026 10:23:49

Published under an exclusive license by AIP Publishing

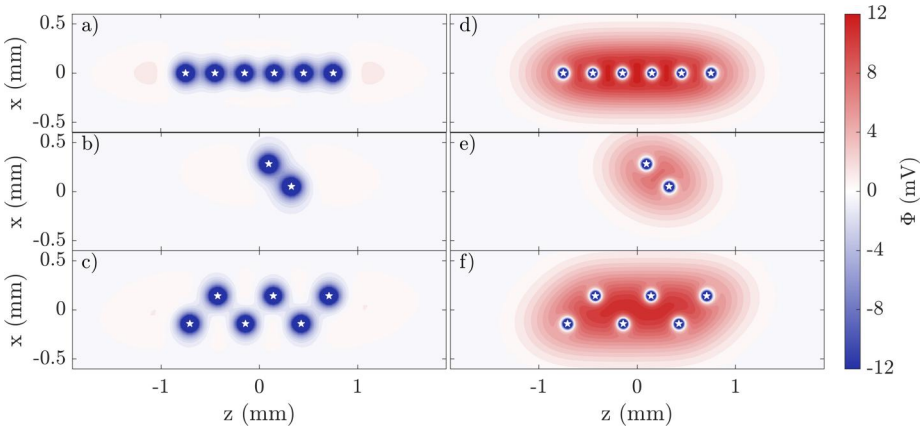


FIG. 17. Electric potential distribution obtained with the potential model in Eq. (6) for the test cases under: (a)–(c) 40 and (d)–(f) 60 Pa gas pressures. The positions of the dust grains are indicated by white stars.

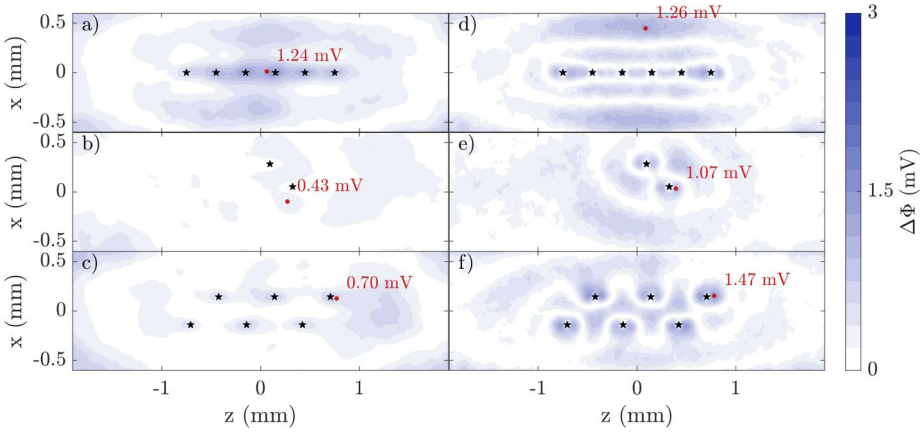


FIG. 18. Absolute difference between the potential distribution obtained with the potential model in Eq. (6) and the data obtained from DRIAD for the test cases at: (a)–(c) 40 and (d)–(f) 60 Pa gas pressures. The positions of the dust grains are represented by black stars. The red dot indicates the position where the maximum difference is reached, while the adjacent red label shows its value.

TABLE IV. Coefficient of Determination (R^2) and Root Mean Squared Error (RMSE) for the test cases.

	40 Pa		60 Pa	
Test case	R^2 (%)	RMSE (mV)	R^2 (%)	RMSE (mV)
1	99.73	0.393	99.79	0.434
2	99.85	0.194	99.78	0.302
3	99.87	0.284	99.94	0.383

$$\vec{F}_{D,d} = -Q_D \sum_{j \neq d}^{N_D} \vec{\nabla} \Phi_j(\vec{r_d}). \tag{9}$$

The force $\vec{F}_z = Q_D \vec{E}_z$ is due to the interaction of the charged dust grain with the axial DC switching electric field E_z, which matches the time-averaged field of the ionization waves used in the DRIAD simulations (see Table I) with $f = 500$ Hz. No external electric field was applied for confinement.

The neutral drag force $\vec{F}_n = -\beta m_D \vec{v}_D$, where $\beta = \frac{4}{3}\delta p R_D^2 \sqrt{8\pi m_n/(k_B T_n)}/m_D$, accounts for the friction due to the collisions of neutral gas atoms on the dust surface and is proportional to the dust velocity $\vec{v}_D$. The coefficient δ represents how the gas atoms are reflected from the dust surface and takes a value of 1.44 for MF spheres.[1] The molecular mass of the neutral gas (neon) m_n is 3.35×10^{-26} kg and the temperature T_n is 25.9 meV.

Finally, the Brownian force $\vec{F}_B = \sqrt{2\beta k_B T_n m_D/\Delta t_D}\vec{\xi}$ represents the random kicks exerted on the dust grains by neutral particles.[16] The dust time step used is $\Delta t_D = 10^{-4}$ s and $\vec{\xi}$ is a vector of normally distributed random numbers between −1 and 1.

This is a simplified model, since the dust charge is assumed to be fixed, while simulations with DRIAD showed that dust charge varies by about 5% for dust particles in close proximity (see Fig. 11). The total time simulated is 50 s (5×10^5 dust time steps). Figure 19 shows snapshots of the simulations at $t = 0$ s (initial positions), $t = 5$ s and $t = 50$ s (final positions) under 40 and 60 Pa gas pressures. Initial positions of dust particles are randomly distributed within a finite region where the dust-dust interaction is active [see Figs. 19(a) and 19(e)], while neutral gas friction damps their response to the interaction forces. In the 40 Pa case, the dust cloud expands [Fig. 19(b)] while dust grains remain clustered for 60 Pa [Fig. 19(f)]. In the final time step, dust particles exhibit the formation of a string-like structure in the 40 Pa case [Fig. 19(c)], with an average interparticle distance of ∼350 μm. This distance falls within the range of interparticle separations observed in the PK-4 experiment (∼200 − 350 μm),[3,26]

16 September 2026 10:23:49

Published under an exclusive license by AIP Publishing

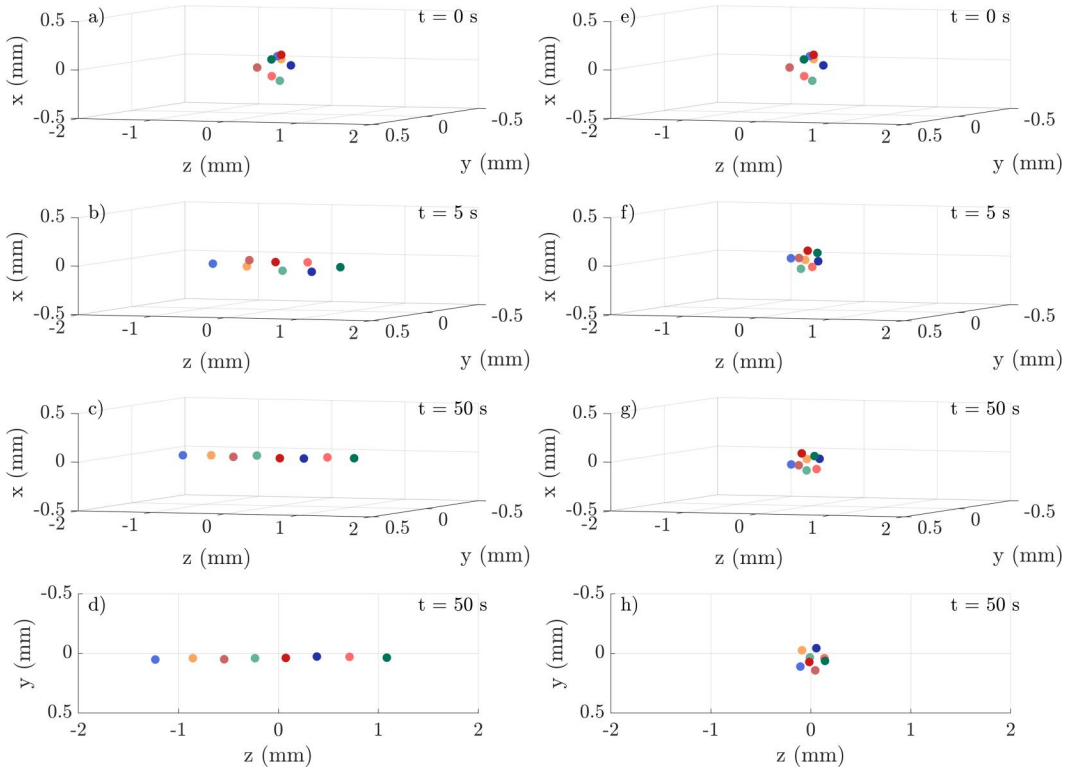


FIG. 19. Snapshots of the simulations for: (a)–(d) 40 and (e)–(h) 60 Pa neutral gas pressures, showing the temporal evolution of the system at: (a) and (e) t = 0 s; (b) and (f) t = 5 s; and (c), (d), (g), and (h) t = 50 s. Panels (d) and (h) represent a view along the *x* axis of the structure at t = 50 s.

indicating that the implemented interaction model produces physically reasonable dust-dust separation scales. For the initial configurations examined, the final chain alignment was robust with respect to the initial particle positions. The resulting interparticle distances varied by only about 20 μm, mainly due to Brownian motion. We note, however, that much larger initial separations could lead to different outcomes because no external confinement is included. In that case, some particles may remain isolated or only partial chains may form if Brownian motion brings a subset of particles close enough to interact. In the 60 Pa case [Fig. 19(f)], the dust cloud does not form an ordered structure, and dust particles remain fixed with random vibrations around their equilibrium positions.

The different behavior of the dust cloud in the two cases can be attributed to the intensity of the axial electric field in the ionization waves (see Fig. 8). Although the values of E_z for both pressures are comparable between ionization waves, the magnitudes of the peaks of E_z in the 40 Pa case ($\sim$2000 V/m) are approximately twice that for 60 Pa ($\sim$1000 V/m) (see Fig. 8). In Ref. 9, the isotropic-to-string phase transition in dusty plasmas was studied experimentally and numerically for different electric fields under microgravity conditions, finding that 6.8 μm-diameter grains under 10 Pa gas pressure form string-like structures at electric fields of about 1800 V/m. In addition, higher electric fields lead to more ordered dust filaments. The dust cloud returned to the isotropic state when the electric field was reduced. The same trend was observed in simulations of dust in the PK-4 environment performed in Ref. 14. Thus, while the present eight-particle simulation is not intended as a direct quantitative reproduction of a specific PK-4 experiment, it is qualitatively consistent with PK-4-related observations in that stronger axial electric fields favor the formation of string-like dust structures. A dedicated quantitative comparison with PK-4 observations is planned for future work, using simulation conditions for which corresponding experimental data are available.

To test this behavior, we analyzed the interaction energy for configurations of two and three dust particles to find configurations that minimize the potential energy. The total interaction energy of a system of N charged particles is $U_{int} = (1/2)\sum_i^N \sum_{j\neq i}^N Q_i \Phi_j(\vec{r}_i)$, where Q_i is the charge of the i-th dust grain and $\Phi_j(\vec{r}_i)$ is the electric potential generated by particle j at the position of particle i. For Φ, we use the potential model given in Eq. (6), generalized to three dimensions, with the corresponding coefficients determined in Sec. V B (Table III). For two dust grains, we vary the interparticle distance (d) and the angle (θ) of their connecting axis with respect to the ion flow direction [Fig. 20(a)]. For three dust grains, we fix two particles along the z-axis separated at a distance d. The third particle is located at the same distance d from the second particle, but at an angle θ relative to the z-axis, as shown in Fig. 20(b). If the system is prone to form a filament, the total interaction energy should naturally be minimized when all three particles are collinear, exhibiting a clear minimum near $\theta = 0^\circ$.

Figure 21 shows the normalized interaction energy of a system of two dust grains as a function of the interparticle distance d and the angle θ. In the 40 Pa case [Fig. 21(a)], two regions of minimum energy appear at $\theta = 0^\circ$ and $\theta = 180^\circ$ at a distance $d_m \approx 460\,\mu$m. At 60 Pa

16 September 2026 10:23:49

Published under an exclusive license by AIP Publishing

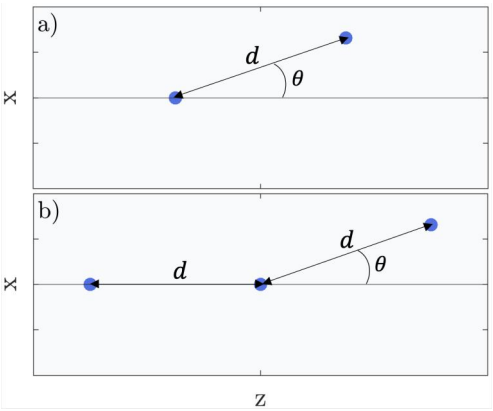


FIG. 20. Schematic representation of the dust configurations used for the interaction energy distribution analysis: (a) two-particle system; (b) three-particle system.

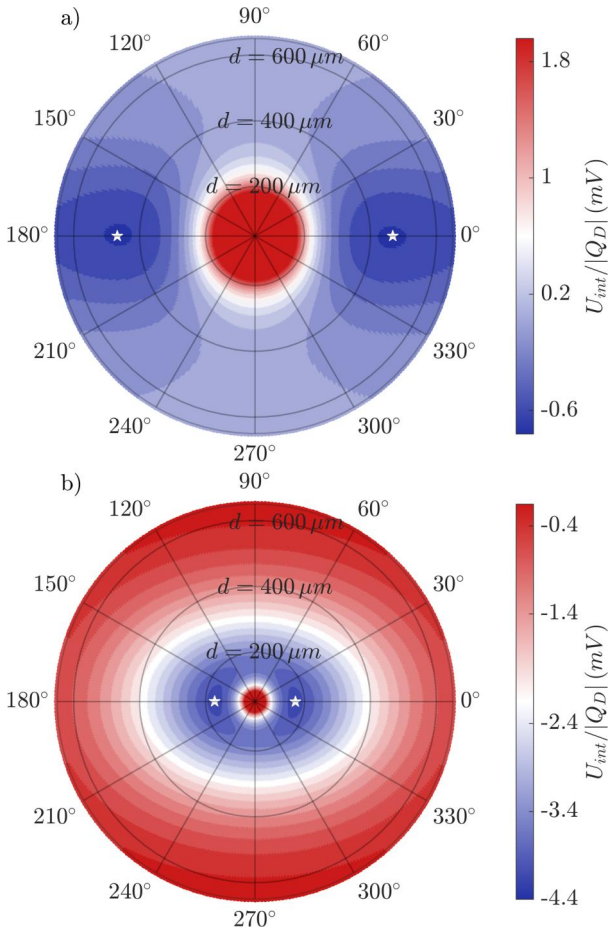


FIG. 21. Interaction energy of a system of two dust grains governed by the potential model Eq. (6) as a function of their separation distance (d) and the angle (θ) between their connecting axis and the direction of the ion flow [see Fig. 20(a)], at: (a) 40 and (b) 60 Pa. All dust grains are assumed to have charge Q_D. Data normalized by $|Q_D|$. The positions of the energy minima are represented by white stars.

[Fig. 21(b)], the interaction energy distribution also exhibits two energy minima near $\theta = 0°$ and $\theta = 180°$, but at a shorter interparticle distance $d_m \approx 175\,\mu$m. This indicates that for a two-particle system, the preferred orientation of the dust grains is parallel to the direction of the ion flow. Figure 22 shows the interaction energy of the three dust grain system as a function of the particle positions. As shown in Fig. 22(a), the system at 40 Pa achieves its minimum energy configuration when $\theta \approx 0°$, which means that all three particles are aligned with the ion flow, forming a string-like structure. In contrast, the minima for the 60 Pa case [Fig. 22(b)] occur near $\theta = 122°$ and $\theta = 238°$. Hence, the equilibrium structure for this scenario is not a filament, but a triangular lattice.

To isolate the role of ion-neutral collisions, the DRIAD simulations were repeated without collisions. Removing collisions changed the ion density distribution and the magnitude of the interaction energy, but not the locations of the energy minima: the 40 Pa case remained near a collinear configuration, whereas the 60 Pa case retained a triangular equilibrium configuration. This indicates that

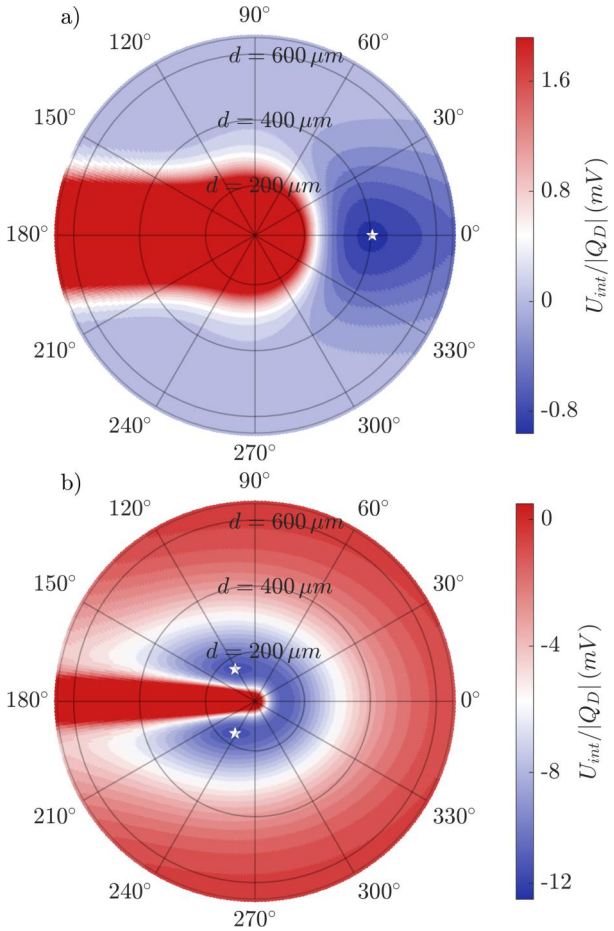


FIG. 22. Interaction energy of a system of three dust grains governed by the potential model Eq. (6) as a function of the interparticle distance (d) and the angle (θ) of the third particle relative to the z-axis [see Fig. 20(b)], at: (a) 40 and (b) 60 Pa. All dust grains are assumed to have charge Q_D. Data normalized by $|Q_D|$. The positions of the energy minima are represented by white stars.

16 September 2026 10:23:49

Published under an exclusive license by AIP Publishing

ion-neutral collisions affect the strength and spatial extent of the ion wake, while its anisotropic structure is governed mainly by the axial electric field characteristic of ionization waves.

VI. CONCLUSIONS

In this work, we developed a compact formulation of the electric potential produced by dust particles and their associated ion wakes under PK-4-like conditions. The model was constructed from the analysis of key features of the potential distribution in the vicinity of dust chains obtained from numerical simulations.

Based on the analysis of the simulation data, the fully independent formulation of the shielded dust potential and Gaussian wake centered on each dust grain [Eq. (4)] was simplified, yielding a compact formulation with a fixed and reduced set of coefficients [Eq. (6)]. This compact formulation, Eq. (6), retains the essential physical features of the dust and ion wake potential while improving computational efficiency and reducing the risk of overfitting. In contrast to previous Gaussian-based formulations, in which the number of fitting coefficients increases with the number of dust particles, the present model retains a fixed set of parameters that remains applicable to different dust configurations.

The model's coefficients (λ, α, σ_x, and σ_z), were determined using a data-driven procedure based on nonlinear fitting and cross-validation applied to a few representative linear dust configurations with varying interparticle distances. The resulting expression for the interaction potential, Eq. (6), accurately reproduces the potential distributions obtained from numerical simulations of the ion dynamics, capturing the essential features of the ion wake in a DC switching electric field.

The predictive capability of the formulation was further validated by showing that the same set of coefficients successfully reproduces the electric potential for diverse dust configurations. This confirms that the parameters retain their validity in different geometries and demonstrates the model's generalizability. The agreement between the model and the simulation data remained high for both training and test cases, with R^2 values exceeding 99%. These results show that the proposed compact formulation provides an accurate and generalizable description of the dust and ion wake electric potential for different dust configurations.

We used the resulting expression for the wake-mediated dust potential to model the dust dynamics without modeling the ions directly. This approach is efficient, as it reduces both the complexity of the code and computational cost compared to explicitly modeling the dust and ions. A simplified simulation of eight dust grains was performed, resulting in a chain-like structure in the 40 Pa case and a compact cluster in the 60 Pa case (Fig. 19). The difference in the dynamical behavior of the dust at the two pressures was explained in terms of interaction energy. In the 40 Pa case, the interaction energy is minimized when the particles are aligned with the ion flow, favoring the formation of string-like structures. In contrast, in the 60 Pa case, the energy minimum is shifted, leading to a non-filamentary equilibrium configuration (Fig. 22). This difference in behavior is mainly due to the greater magnitude of the electric field associated with the ionization waves in the 40 Pa case. This underscores the importance of the nature of the ionization waves for a given set of plasma conditions in the formation of strings and the ER behavior.

The model used here is applicable to alternating electric fields, where a symmetric ion wake forms on both sides of a dust grain. In unidirectional electric fields, such as those present in the plasma sheath of a capacitively coupled plasma cell, the wake forms predominantly on one side of the dust grain.[22] Therefore, the present model must be adapted to account for the resulting asymmetries.

One limitation of the simplified dust dynamics model presented in Sec. V D is that it neglected the variations of the dust charge in proximity to other grains (Fig. 11). This variation will be taken into account in future work, in which we plan to model large populations of dust grains for various PK-4 plasma conditions to help explain the experimentally observed structures.

ACKNOWLEDGEMENTS

The authors gratefully acknowledge support from the U.S. Department of Energy, Office of Science, Office of Fusion Energy Sciences under Award No. DE-SC-0021334 and the National Science Foundation Grant No. PHY 2308743. Peter Hartmann gratefully acknowledges the hardware support of the NVIDIA Corporation under the NVIDIA GPU Grant Program.

AUTHOR DECLARATIONS

Conflict of Interest

The authors have no conflicts to disclose.

Author Contributions

Diana Jimenez Marti: Conceptualization (lead); Formal analysis (lead); Methodology (lead); Software (equal); Visualization (lead); Writing – original draft (lead). **Benny Rodriguez Saenz:** Conceptualization (supporting); Methodology (supporting); Software (equal); Writing – review & editing (equal). **Peter Hartmann:** Methodology (supporting); Software (supporting); Writing – review & editing (supporting). **Evdokiya Kostadinova:** Conceptualization (supporting); Funding acquisition (equal); Writing – review & editing (supporting). **Truell Hyde:** Funding acquisition (equal); Writing – review & editing (supporting). **Lorin Swint Matthews:** Data curation (equal); Methodology (supporting); Resources (lead); Software (supporting); Supervision (lead); Writing – review & editing (equal).

DATA AVAILABILITY

The data that support the findings of this study are available from the corresponding author upon reasonable request.

REFERENCES

[1]A. Melzer, *Physics of Dusty Plasmas: An Introduction*, Lecture Notes in Physics Vol. 962 (Springer, Cham, 2019).
[2]S. Mitic, B. Klumov, S. Khrapak, and G. Morfill, "Three-dimensional complex plasma structures in a combined radio frequency and direct current discharge," Phys. Plasmas **20**, 043701 (2013).
[3]M. Pustylnik, B. Klumov, M. Rubin-Zuzic, A. Lipaev, V. Nosenko, D. Erdle, A. Usachev, A. Zobnin, V. Molotkov, G. Joyce *et al.*, "Three-dimensional structure of a string-fluid complex plasma," Phys. Rev. Res. **2**, 033314 (2020).
[4]H. Thomas, G. Morfill, V. Demmel, J. Goree, B. Feuerbacher, and D. Möhlmann, "Plasma crystal: Coulomb crystallization in a dusty plasma," Phys. Rev. Lett. **73**, 652 (1994).
[5]J. Chu and I. Lin, "Direct observation of Coulomb crystals and liquids in strongly coupled RF dusty plasmas," Phys. Rev. Lett. **72**, 4009 (1994).
[6]J. Pieper, J. Goree, and R. Quinn, "Experimental studies of two-dimensional and three-dimensional structure in a crystallized dusty plasma," J. Vac. Sci. Technol. A **14**, 519 (1996).

16 September 2026 10:23:49

Published under an exclusive license by AIP Publishing

[7]V. Fortov, G. Morfill, O. Petrov, M. Thoma, A. Usachev, H. Hoefner, A. Zobnin, M. Kretschmer, S. Ratynskaia, M. Fink *et al.*, "The project 'Plasmakristall-4'(PK-4)—A new stage in investigations of dusty plasmas under microgravity conditions: First results and future plans," Plasma Phys. Controlled Fusion **47**, B537 (2005).
[8]A. Ivlev, G. Morfill, H. Thomas, C. Räth, G. Joyce, P. Huber, R. Kompaneets, V. Fortov, A. Lipaev, V. Molotkov *et al.*, "First observation of electrorheological plasmas," Phys. Rev. Lett. **100**, 095003 (2008).
[9]A. V. Ivlev, P. C. Brandt, G. E. Morfill, C. Rath, H. M. Thomas, G. Joyce, V. E. Fortov, A. M. Lipaev, V. I. Molotkov, and O. F. Petrov, "Electrorheological complex plasmas," IEEE Trans. Plasma Sci. **38**, 733 (2010).
[10]A. Melzer, V. Schweigert, I. Schweigert, A. Homann, S. Peters, and A. Piel, "Structure and stability of the plasma crystal," Phys. Rev. E **54**, R46 (1996).
[11]L. Couëdel, V. Nosenko, M. Rubin-Zuzic, S. Zhdanov, Y. Elskens, T. Hall, and A. Ivlev, "Full melting of a two-dimensional complex plasma crystal triggered by localized pulsed laser heating," Phys. Rev. E **97**, 043206 (2018).
[12]L. Couëdel, S. Zhdanov, A. Ivlev, V. Nosenko, H. Thomas, and G. Morfill, "Wave mode coupling due to plasma wakes in two-dimensional plasma crystals: In-depth view," Phys. Plasmas **18**, 083707 (2011).
[13]P. Hartmann, M. Rosenberg, Z. Juhasz, L. S. Matthews, D. L. Sanford, K. Vermillion, J. Carmona-Reyes, and T. W. Hyde, "Ionization waves in the PK-4 direct current neon discharge," Plasma Sources Sci. Technol. **29**, 115014 (2020).
[14]L. S. Matthews, K. Vermillion, P. Hartmann, M. Rosenberg, S. Rostami, E. Kostadinova, T. Hyde, M. Pustylnik, A. Lipaev, A. Usachev *et al.*, "Effect of ionization waves on dust chain formation in a DC discharge," J. Plasma Phys. **87**, 905870618 (2021).
[15]V. Schweigert, I. Schweigert, A. Melzer, A. Homann, and A. Piel, "Alignment and instability of dust crystals in plasmas," Phys. Rev. E **54**, 4155 (1996).
[16]L. S. Matthews, D. L. Sanford, E. G. Kostadinova, K. S. Ashrafi, E. Guay, and T. W. Hyde, "Dust charging in dynamic ion wakes," Phys. Plasmas **27**, 023703 (2020).
[17]K. Qiao, J. Kong, E. V. Oeveren, L. S. Matthews, and T. W. Hyde, "Mode couplings and resonance instabilities in dust clusters," Phys. Rev. E **88**, 043103 (2013).
[18]A. Melzer, A. Schella, and M. Mulsow, "Nonequilibrium finite dust clusters: Connecting normal modes and wakefields," Phys. Rev. E **89**, 013109 (2014).
[19]O. Ishihara, S. Vladimirov, and N. Cramer, "Effect of a dipole moment on the wake potential of a dust grain in a flowing plasma," Phys. Rev. E **61**, 7246 (2000).
[20]T. Röcker, A. Ivlev, R. Kompaneets, and G. Morfill, "Mode coupling in two-dimensional plasma crystals: Role of the wake model," Phys. Plasmas **19**, 033708 (2012).
[21]R. Kompaneets, "Complex plasmas: Interaction potentials and non-Hamiltonian dynamics," Ph.D. thesis (LMU, 2007).
[22]K. Vermillion, R. Banka, A. Mendoza, B. Wyatt, L. Matthews, and T. Hyde, "Interacting dust grains in complex plasmas: Ion wake formation and the electric potential," Phys. Plasmas **31**, 073701 (2024).
[23]A. Mendoza, D. Jiménez Martí, L. S. Matthews, B. Rodríguez Saenz, P. Hartmann, E. Kostadinova, M. Rosenberg, and T. W. Hyde, "Ion density waves driving the formation of filamentary dust structures," Phys. Plasmas **32**, 023705 (2025).
[24]M. Pustylnik, M. Fink, V. Nosenko, T. Antonova, T. Hagl, H. Thomas, A. Zobnin, A. Lipaev, A. Usachev, V. Molotkov *et al.*, "Plasmakristall-4: New complex (dusty) plasma laboratory on board the international space station," Rev. Sci. Instrum. **87**, 093505 (2016).
[25]V. Fortov, A. Ivlev, S. Khrapak, A. Khrapak, and G. Morfill, "Complex (dusty) plasmas: Current status, open issues, perspectives," Phys. Rep. **421**, 1–103 (2005).
[26]S. Mitic, M. Pustylnik, D. Erdle, A. Lipaev, A. Usachev, A. Zobnin, M. H. Thoma, H. M. Thomas, O. Petrov, V. Fortov *et al.*, "Long-term evolution of the three-dimensional structure of string-fluid complex plasmas in the PK-4 experiment," Phys. Rev. E **103**, 063212 (2021).
[27]E. Gehr, A. Terrell, K. Vermillion, A. Mendoza, B. Andrew, D. Jimenez Marti, E. Kostadinova, P. Hartmann, L. Matthews, and T. Hyde, "Structural states of filamentary microgravity dusty plasma," arXiv:2505.14576 (2025).
[28]A. Melzer, V. Schweigert, and A. Piel, "Transition from attractive to repulsive forces between dust molecules in a plasma sheath," Phys. Rev. Lett. **83**, 3194 (1999).
[29]I. H. Hutchinson, "Ion collection by a sphere in a flowing plasma: I. Quasineutral," Plasma Phys. Controlled Fusion **44**, 1953–1977 (2002).
[30]L. Couëdel, B. Rodriguez Saenz, D. Jimenez Marti, and L. Matthews, "Ion wakes in two-dimensional complex plasma crystals," Phys. Plasmas **33**, 053701 (2026).
[31]MathWorks, *Overfitting* (MathWorks, 2025).
[32]J. N. K. Steven and L. Brunton, *Data-Driven Science and Engineering. Machine Learning, Dynamical Systems, and Control* (Cambridge University Press, 2002).
[33]MathWorks, *Coefficient of determination (R-squared)* (MathWorks, 2025).
[34]E. G. Kostadinova *et al.*, "Liquid plasma crystals on the ISS," AIAA Paper No. 2023-2615, 2023.

16 September 2026 10:23:49

Published under an exclusive license by AIP Publishing